coatings

MDPI

Article

Effect of NiO Nanoparticle Addition on the Structural, Microstructural, Magnetic, Electrical, and Magneto-Transport Properties of $La_{0.67}Ca_{0.33}MnO_3$ Nanocomposites

Lik Nguong Lau [1], Kean Pah Lim [1,*], See Yee Chok [1], Amirah Natasha Ishak [1], Xiao Tong Hon [1], Yan Jing Wong [1], Mohd Mustafa Awang Kechik [1], Soo Kien Chen [1], Noor Baa'yah Ibrahim [2], Muralidhar Miryala [3], Masato Murakami [3] and Abdul Halim Shaari [1]

[1] Superconductor and Thin Film Laboratory, Department of Physics, Faculty of Science, Universiti Putra Malaysia, UPM, Serdang 43400, Selangor Darul Ehsan, Malaysia; lau7798@gmail.com (L.N.L.); seeyeejh@gmail.com (S.Y.C.); amirahnatasha.ir@gmail.com (A.N.I.); xiaotong961229@gmail.com (X.T.H.); wongyjphy@gmail.com (Y.J.W.); mmak@upm.edu.my (M.M.A.K.); chensk@upm.edu.my (S.K.C.); ahalim@upm.edu.my (A.H.S.)

[2] Department of Applied Physics, Faculty of Science and Technology, Universiti Kebangsaan Malaysia, UKM, Bangi 43600, Selangor Darul Ehsan, Malaysia; baayah@ukm.edu.my

[3] Shibaura Institute of Technology, 3 Chome-7-5 Toyosu, Koto, Tokyo 135-8548, Japan; miryala1@shibaura-it.ac.jp (M.M.); masatomu@shibaura-it.ac.jp (M.M.)

* Correspondence: limkp@upm.edu.my

Abstract: Incorporation of the secondary oxide phase into the manganite composite capable of enhancing low-field magnetoresistance (LFMR) for viability in high-performance spintronic applications. Polycrystalline $La_{0.67}Ca_{0.33}MnO_3$ (LCMO) was prepared via the sol–gel route in this study. The structural, microstructural, magnetic, electrical, and magneto-transport properties of $(1-x)$ LCMO: x NiO, x = 0.00, 0.05, 0.10, 0.15 and 0.20 were investigated in detail. The X-ray diffraction (XRD) patterns showed the coexistence of LCMO and NiO in the composites. The microstructural analysis indicated the amount of NiO nanoparticles segregated at the grain boundaries or on the surface of LCMO grains increased with the increasing secondary phase content. LCMO and NiO still retained their individual magnetic phase as observed from AC susceptibility (ACS) measurement. This further confirmed that there is no interfacial diffusion reaction between these two compounds. The NiO nanoparticle acted as a barrier to charge transport and caused an increase in resistivity for composite samples. The residual resistivity due to the grain/domain boundary is responsible for the scattering mechanism in the metallic region as suggested by the theoretical model fitting, $\rho(T) = \rho_0 + \rho_2 T^2 + \rho_{4.5} T^{4.5}$. The magnetoresistance values of LCMO and its composites were found to increase monotonically with the decrease in temperature. Hence, the LFMR was observed. Nonetheless, the slight reduction of LFMR in composites was attributed to the thick boundary layer created by NiO and impaired the spin polarised tunnelling process.

Keywords: fitting; grain boundary; LFMR; sol–gel

Citation: Lau, L.N.; Lim, K.P.; Chok, S.Y.; Ishak, A.N.; Hon, X.T.; Wong, Y.J.; Awang Kechik, M.M.; Chen, S.K.; Ibrahim, N.B.; Miryala, M.; et al. Effect of NiO Nanoparticle Addition on the Structural, Microstructural, Magnetic, Electrical, and Magneto-Transport Properties of $La_{0.67}Ca_{0.33}MnO_3$ Nanocomposites. *Coatings* **2021**, *11*, 835. https://doi.org/10.3390/coatings11070835

Academic Editor: Joe Sakai

Received: 22 June 2021
Accepted: 9 July 2021
Published: 11 July 2021

1. Introduction

The hole-doped manganites with a general formula of $RE_{1-x}A_xMnO_3$, where RE is a rare earth ion (RE = La, Nd, Pr) and A is a divalent alkaline earth metal ion (B = Ba, Sr, Ca) have attracted considerable research interest due to their intriguing properties. The correlation between spin, charge, orbital, and lattice degrees of freedom in manganites has been extensively studied [1–3]. Magnetoresistance effect is an important phenomenon to be utilised by magnetic field sensing elements in novel technological devices. It is described by the change of resistance when a conductor is placed under the influence of a magnetic field. The discovery of colossal magnetoresistance (CMR) on manganites has earned them a spot in spintronic technologies such as memory recording applications and magnetic field

sensors [4]. Perovskite manganites exhibit CMR in the vicinity of metal-insulator transition and ferromagnetic–paramagnetic transition [5]. The electrical conduction and magnetism in manganites can be explained by the double exchange (DE) mechanism between pairs of Mn^{3+} and Mn^{4+} [6].

The CMR effects of perovskite manganites are grouped into two categories, namely intrinsic and extrinsic magnetoresistance, respectively [7]. The intrinsic magnetoresistance is only expressive at high saturation magnetic field about several teslas while the extrinsic magnetoresistance is significantly higher in low magnetic fields [8]. A high-efficiency magnetoresistive material should be able to respond at low magnetic fields for its viability in practical spintronic applications [9]. The extrinsic magnetoresistance is attributed to the spin polarised tunnelling, and it can be achieved by the natural or artificial grain boundaries in manganites [10,11]. Therefore, an introduction of the secondary oxide phase into the manganite system has been adopted by the scientific community as its capability to enhance low field magnetoresistance (LFMR). This approach is favoured by recent research works and has proven as an effective attempt to improve the LFMR as demonstrated by $La_{0.8}Sr_{0.2}MnO_3$:NiO [12], $La_{0.7}Sr_{0.3}MnO_3$: $SrFe_{12}O_{19}$ [13], $La_{0.67}Ca_{0.33}MnO_3$: Sm_2O_3 [14], $La_{0.7}Ca_{0.2}Sr_{0.1}MnO_3$: MgO [15], $La_{0.7}Ca_{0.3}MnO_3$: Al_2O_3 [16], $La_{0.7}Sr_{0.3}MnO_3$: AZO [17] and $La_{0.7}Sr_{0.3}MnO_3$: ZnO [18].

The understanding of the secondary oxide phase in the manganite composites development is important in designing high-performance spintronic applications. Nickel oxide (NiO) is an insulator with a high melting point and proved to be an excellent candidate as the secondary phase in manganite composites [19]. The NiO nanoparticle has successfully enhanced the LFMR of $Pr_{0.67}Sr_{0.33}MnO_3$ composites prepared by solid-state reaction [20]. Additionally, Ning et al. incorporated NiO into the $La_{0.7}Ca_{0.3}MnO_3$ nanocomposite thin films and significantly enhanced the LFMR over a broad temperature range by tuning the microstructures [21]. Eshraghi et al. described that the NiO doping influenced LFMR in $La_{0.8}Sr_{0.2}MnO_3$:NiO composites [12]. From their study, the composites with high NiO content demonstrated the reduction in LFMR, originating from the substitution of Ni^{2+} with the Mn^{3+} and causing the magnetic dilution. Besides the concentration of the secondary phase, the spin polarised tunnelling responsible for LFMR could also be restricted by the nanosized parent compound, which was proposed in our previous work for LCMO: Al_2O_3 [22].

In this work, we prepared $(1-x)$ LCMO: x NiO (x = 0.00, 0.05, 0.10, 0.15 and 0.20) by the sol–gel method. The effects of NiO nanoparticle addition on the structural, microstructural, magnetic, electrical, and magneto-transport properties were systematically examined. To the best of our knowledge, there is no up-to-date literature on the sol–gel synthesised LCMO:NiO nanocomposite. Hence, this work is important in providing a novel understanding of manganite composites.

2. Materials and Methods

$(1-x)$ LCMO: x NiO composite samples were prepared by two stages, which are the synthesis of LCMO via sol–gel route and the addition of NiO nanoparticles. For the preparation of LCMO, the stoichiometric ratios of $La(NO_3)_3{\cdot}6H_2O$ (Alfa Aesar, Heysham, UK; 99.99%), $Ca(NO_3)_2{\cdot}4H_2O$ (Alfa Aesar, Heysham, UK; 99.98%) and $Mn(NO_3)_2{\cdot}4H_2O$ (Merck, Darmstadt, Germany; ≥98.5%) were dissolved in an appropriate amount of distilled water under a constant stirring. Citric acid and ethylene glycol were later added to the precursor solution as a chelating agent and a dispersant (polymerization of metal ions), respectively. The mixed solution was left for 24 h and stirred constantly at 70 °C until it turned into a yellowish gel. The gel was further dried in an oven at 120 °C to remove the moisture. It was ground into fine powder in an agate mortar before being calcined at 500 °C for 5 h. Later, the powder was pre-sintered at 800 °C for 6 h to facilitate the formation of the LCMO phase. Next, the LCMO powder was added with different contents of NiO (Sigma Aldrich, St. Louis, MO, USA; 99.8%) nanoparticle (<50 nm) at x = 0.00, 0.05, 0.10, 0.15 and 0.20. These mixed powders were ground and pressed into pellets, then sintered at 800 °C for 2 h.

All samples were evaluated by an X-ray fluorescence spectrometer (XRF, Shimadzu EDX-720, Shimadzu Corporation, Kyoto, Japan) and energy-dispersive X-ray spectrometer (EDX, Max 20, Oxford Instruments, Abingdon, UK) to confirm the existence of a secondary phase (NiO) in the composites. The structural characterisation was carried out by an X-ray diffractometer (XRD, X'Pert Pro PW 3040, Malvern Panalytical, Malvern, UK) and Rietveld analysis was performed by HighScore Plus software. The surface morphologies and microstructures were observed by a field emission scanning electron microscope (FESEM, FEI Nova NanoSEM 230, Thermo Fisher Scientific, Waltham, MA, USA). AC susceptibility was measured by an AC susceptometer (ACS, CryoBIND T, CryoBIND, Zagreb, Croatia) in a magnetic field of 5 Oe at 219 Hz to determine the Curie temperature (T_C). The temperature dependence of the resistivity and magneto-transport were assessed by standard four-point probe method using a Hall effect measurement system (HMS, Lakeshore 7604, Lake Shore Cryotronics, Westerville, OH, USA) from 80 K to 300 K.

3. Results and Discussion

X-ray diffraction patterns of the samples with different NiO contents are depicted in Figure 1a. Standard XRD peaks for LCMO and NiO are illustrated in red and blue vertical lines, respectively. All samples exhibited a strong orientation towards (121) plane direction. This is contributed by the dominant plane orientation of their parent compound (LCMO). Minor peaks corresponding to NiO in the composites were observed and the relative peak intensity is gradually increased with the increasing NiO content. All peaks were indexed with LCMO and NiO phases, indicating the coexistence of the two chemically separated phases. Figure 1b illustrates the Rietveld XRD pattern of the pure LCMO phase. The blue circle is the diffraction data obtained from the experiment, the black solid line is the calculated result, the green vertical line represents the diffraction peak position of the LCMO phase, the red solid line is the difference between the experimental value and the calculated value. The experimental data are considered to fit well with calculated data as given by the low residual values of R_{WP} and χ^2. The refinement parameters of $(1-x)$ LCMO: x NiO (x = 0.00, 0.05, 0.10, 0.15 and 0.20) are summarised in Table 1. There is no significant change in the lattice constants (a, b, c, V) of LCMO composites. This implies that NiO is segregated on the surface of LCMO grains or at the grain boundaries [14,23]. The average crystallite size, D was calculated by Scherrer's equation below and gathered in Table 2:

$$D = \frac{0.9\,\lambda}{\beta\,\cos\theta} \quad (1)$$

where $\beta = \beta_{sample} - \beta_{instrumental}$, β is the line broadening at half of the maximum intensity (FWHM), λ is the X-ray wavelength (1.5406 Å) and θ is the position of the most intense diffraction peak. The calculated average crystallite size based on the (121) peak is found to be in the range of 35–39 nm as listed in Table 2. The results further confirmed that there is no reaction between NiO and LCMO as the changes in crystallite size are negligible.

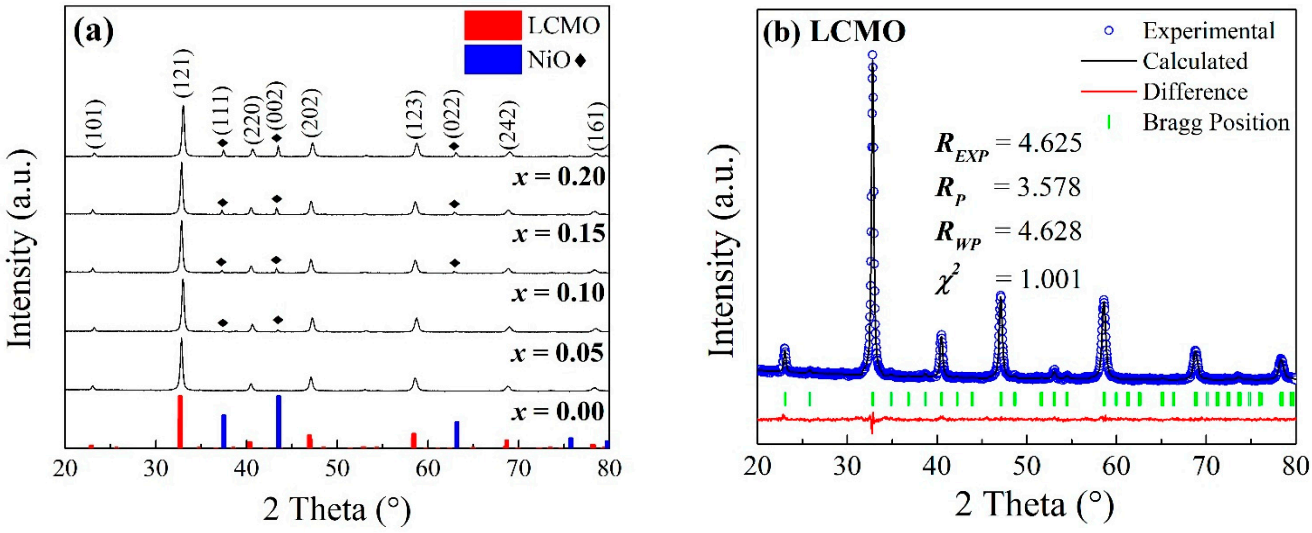

Figure 1. (**a**) XRD patterns of LCMO:NiO composites. (**b**) Rietveld refinement of LCMO.

Table 1. Rietveld refinement data of pure LCMO and LCMO:NiO composites.

Sample	**LCMO**				
Ref. code			98-006-5295		
Structure type			Orthorhombic		
Space group			Pnma (62)		
NiO content, *x*	0.00	0.05	0.10	0.15	0.20
a (Å)	5.454	5.454	5.453	5.452	5.454
b (Å)	7.710	7.704	7.717	7.705	7.706
c (Å)	5.462	5.473	5.458	5.467	5.473
V (Å^3)	229.688	229.975	229.676	229.684	230.334
Mn1-O1 (Å)	1.930 (19)	1.932(14)	1.929 (22)	1.931 (17)	1.932 (18)
Mn1-O1 (Å)	1.974 (19)	1.977 (14)	1.973 (23)	1.975 (17)	1.977 (19)
Mn1-O2 (Å)	1.954 (13)	1.952 (5)	1.955 (19)	1.953 (8)	1.953 (8)
Mn1-O1-Mn1 (°)	162.6 (3)	162.6 (4)	162.5 (6)	162.6 (6)	162.58 (6)
Mn1-O2-Mn1 (°)	161.2 (7)	161.1 (9)	161.2 (7)	161.2 (7)	161.1 (7)
R_{EXP} (%)	4.625	4.178	3.843	3.757	3.511
R_P (%)	3.578	3.324	3.064	3.003	2.853
R_{WP} (%)	4.628	4.317	3.917	3.818	3.546
Goodness of fit, χ^2	1.001	1.068	1.039	1.032	1.020
Sample			NiO		
Ref. code			98-000-8168		
Structure type			Cubic		
Space group			Fm-3m (225)		
a (Å)	-	4.179	4.177	4.177	4.179
b (Å)	-	4.179	4.177	4.177	4.179
c (Å)	-	4.179	4.177	4.177	4.179
V (Å^3)	-	72.97	72.86	72.86	72.96

Table 2. The *D*, T_{MI}, and *MR* (%) at 80 K for sample *x* = 0.00, 0.05, 0.10, 0.15 and 0.20.

x	*D* (nm)	T_{C1} (K)	T_{C2} (K)	T_{MI} (K)	ΔT (K)	*MR* (%) at 80 K	
						2 kOe	10 kOe
0.00	35.8	289	-	172	117	20.70	29.41
0.05	35.9	293	179	116	177	16.48	26.70
0.10	37.5	287	173	98	189	14.09	25.04
0.15	38.7	291	174	<80	-	15.76	27.84
0.20	35.3	292	175	<80	-	14.53	26.83

To analyse the addition of NiO nanoparticles on the microstructure of LCMO, the typical FESEM micrographs and grain size distributions of $(1-x)$ LCMO: x NiO (x = 0.00, 0.10, 0.20) composites are shown in Figure 2a–c. Energy-dispersive X-ray (EDX) spectra are also included in Figure 2. The grain size distribution was depicted by 100 grains randomly picked from the FESEM micrographs. All samples were observed to compose with an irregular shape of grains, and it was found that the grain size of pure LCMO sample is in the range of 40–180 nm with 98.1 nm as the mean grain size. The average grain size of LCMO is ~3 times larger than its crystallite size, indicating the grain is consisting of several crystallites. The difference between grain and crystallite sizes is ascribed to the congregation or structure defects (vacancies, dislocations and stacking faults) of crystallite domains [24]. The grain size distribution is observed to skew to the left with the increasing NiO content. As a result, the mean grain size of samples reduced to ~70 nm with the addition of secondary phase (NiO). The reduction of average grain size in composites suggested that the NiO nanoparticle (<50 nm) was mainly segregated at the grain boundaries or on the surface of LCMO grains, which is in line with the XRD results. This also confirms the composite structure for the samples obtained in this work. The presence of La, Ca, Mn, O and Ni were confirmed by the EDX characterization and this supports the existence of NiO in the composites as demonstrated by the XRF results (not shown).

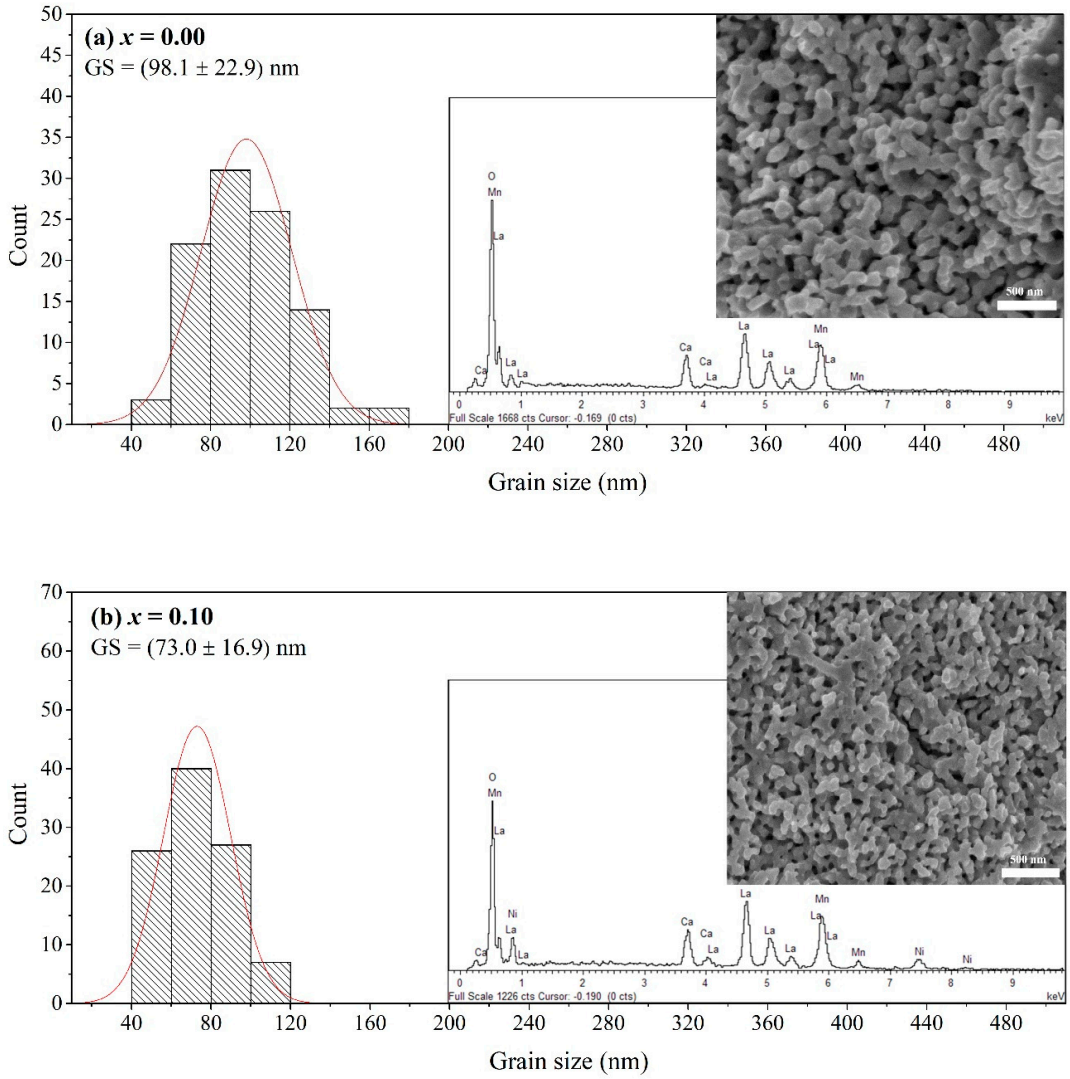

Figure 2. *Cont.*

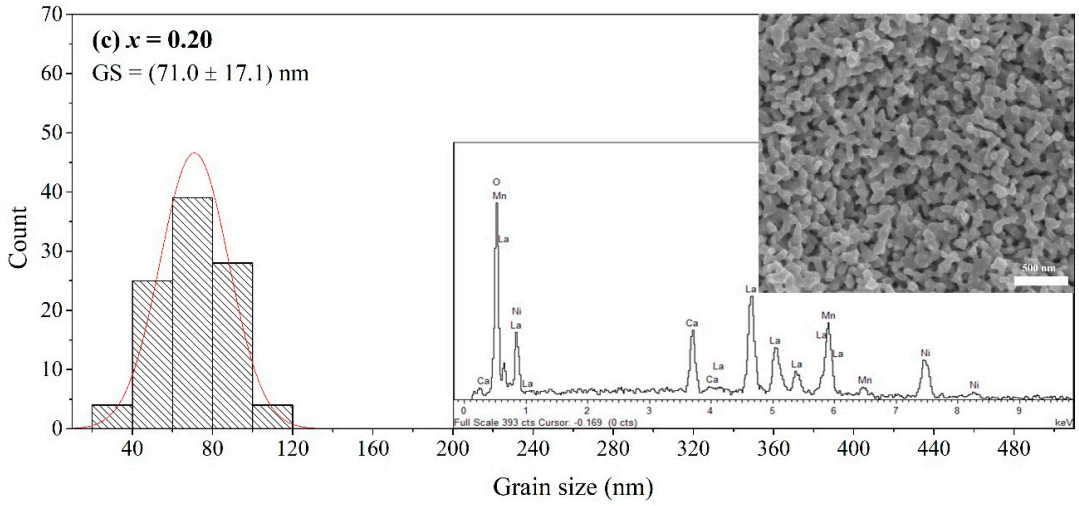

Figure 2. Grain size distribution histograms, FESEM micrographs and EDX spectra of (**a**) x = 0.00, (**b**) x = 0.10 and (**c**) x = 0.20.

The magnetic properties of the samples were studied by the temperature dependence of AC susceptibility (ACS) measurement. All samples showed the ferromagnetic (FM)–paramagnetic (PM) transition as the temperature increases from 80 K to 330 K. The transition is demonstrated by a rapid drop of susceptibility until it reaches a minimum value (close to 0). The *Tc* can be identified from the inflection point of $d\chi'/dT$ versus T plot. Figure 3 shows the temperature dependence of the real part of AC susceptibility for LCMO:NiO composites. The T_C of the pure LCMO was observed at 289 K and was denoted as T_{C1} in Table 2. This value is higher than the value reported by Xia et al. in $La_{0.7}Ca_{0.3}MnO_3$ nanoparticle (268 K) [25]. The discrepancy can be attributed to the loss of long-range ferromagnetic ordering and the presence of magnetic disordered grain boundary layers in previously reported LCMO nanoparticles (<50 nm). The grain size of LCMO in this work is larger (98 nm), thus it has a higher value of T_C [26,27]. The T_{C1} values recorded by the composite samples are in the range of 287–293 K. This indicates that the LCMO perovskite lattice remained intact, and no substitution occurred or formation of the new phase. The difference in T_C of composites is insignificant by considering the FM–PM transition as an intrinsic and intragrain behaviour [28]. Nonetheless, there is an increase in the transition width and occurrence of T_{C2} for the LCMO:NiO composites. This can be ascribed to the presence of the antiferromagnetic material which is NiO nanoparticles at the grain boundaries and/or grain surfaces, where a similar behaviour was reported in $La_{0.8}Sr_{0.2}MnO_3$:NiO composites [12]. Both T_{C1} and T_{C2} do not experience significant change with the increasing content of NiO. Therefore, we can deduce that LCMO and NiO still retain their individual magnetic phase in the composites and there is no interfacial reaction between these two phases.

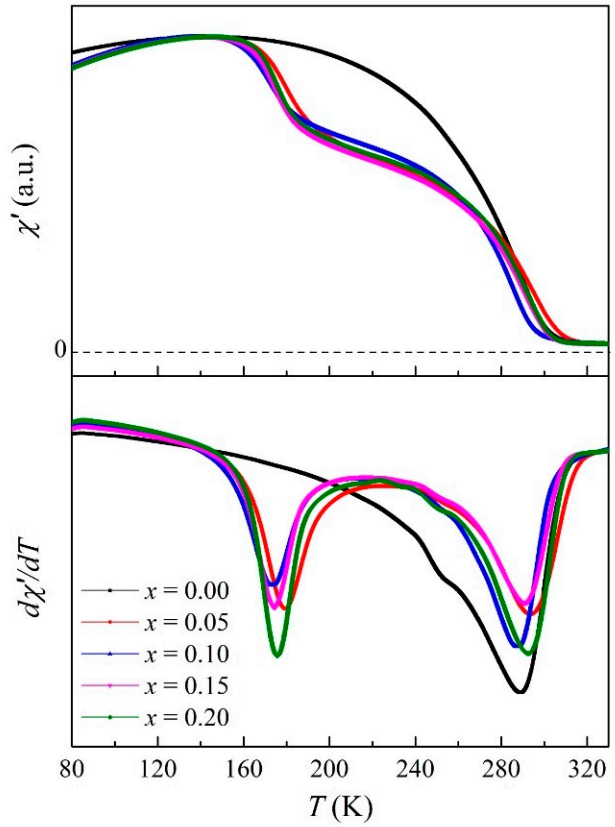

Figure 3. Temperature dependence of AC susceptibility for LCMO:NiO composites.

Figure 4 shows the temperature dependence of the resistivity at various fields (0 kOe, 2 kOe and 10 kOe) for the LCMO:NiO composites. It is observed that the resistivity of the samples increases with the concentration of NiO. This can be attributed to the increasing amount of NiO nanoparticles segregated at the grain boundaries or on the LCMO grain surface, and it contributes to the scattering enhancement near the grain boundaries. Most samples in this work (x = 0.00, 0.05 and 0.10) showed a distinct metal–insulator transition in the range of 80–180 K. The metal–insulator transition temperature (T_{MI}) shifted to a higher temperature under the influence of a magnetic field. This effect is attributed to the alignment of localised spin in manganite and leads to the reduction in electron scattering, thus enhance the DE coupling in the metallic region [22,29]. Additionally, the T_{MI} appeared to shift towards the lower temperature region with the increasing content of NiO in LCMO composites. The same behaviour was reported in our previous work for LCMO: Al_2O_3 composites [22]. This shift is caused by the segregation of NiO nanoparticles near the LCMO grains or grain boundaries of the composites. The NiO nanoparticle acted as a barrier to charge transport and caused an increase in the resistivity, as well as the dilution to the DE interaction [30]. The decrease of T_{MI} values in composite samples also indicates that the extrinsic transport behaviour originates from the interface and grain boundary effects [11,31]. The transport behaviour of the composite can be explained by the parallel network of good and bad conduction channels, also known as the two-channel conduction model [13,18,32]. The charge transport in the pure LCMO sample is contributed by the direct contact between LCMO grains. In contrast, the presence of insulating NiO nanoparticles near the grain boundaries in composites results in the increase of resistivity and the shift of T_{MI} towards the lower temperature region. Magnetic and electrical behaviours are important physical properties of manganite materials. From the literature, the values of T_C and T_{MI} are close to each other for bulk manganites [33]. Nevertheless, this differs for nanocrystalline samples as demonstrated by our work here. The difference between T_{C1} and T_{MI} is given as ΔT and summarised in Table 2. The ΔT value is getting greater

with the NiO content. This is because the electrical behaviour (T_{MI}) is dependent on the microstructural properties such as grain size and grain boundary, while the magnetic behaviour (T_{C1}) is a cumulative effect of intrinsic properties in manganites [24,34].

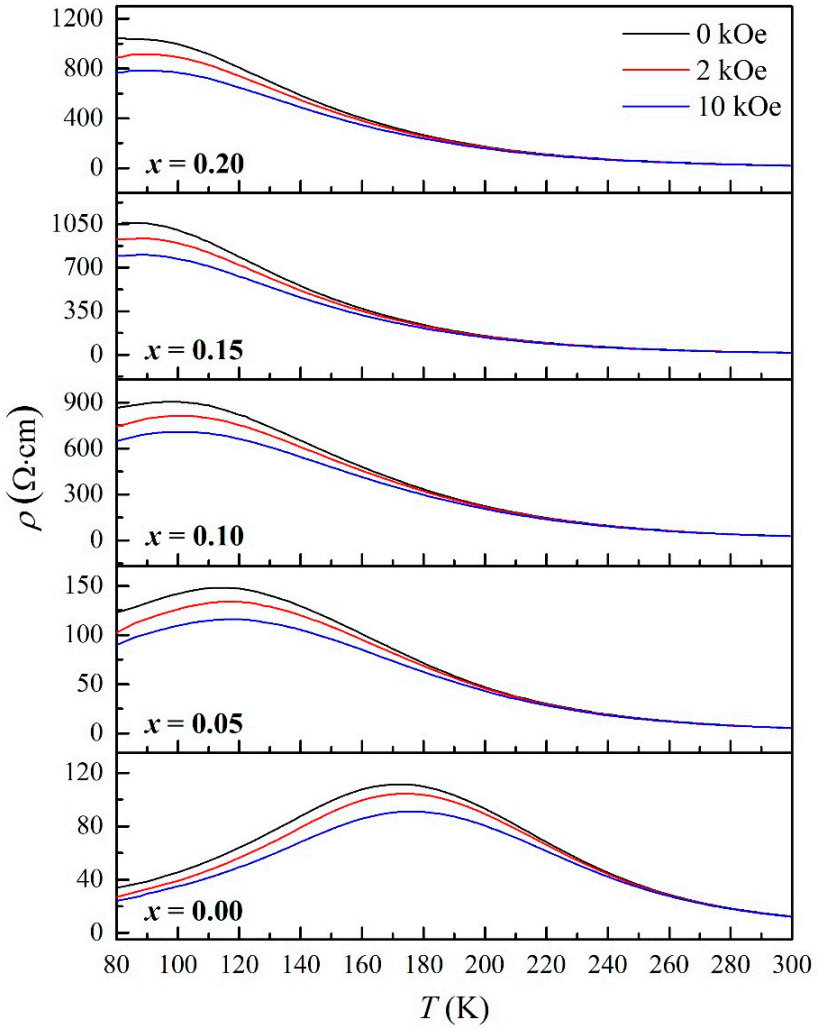

Figure 4. Temperature dependence of the resistivity at various fields for the pure LCMO and its composites.

To gain insight into the different scattering mechanisms in the metallic region ($T < T_{MI}$), the electrical resistivity data were fitted with the equation below [27,35,36]:

$$\rho(T) = \rho_0 + \rho_2 T^2 + \rho_{4.5} T^{4.5} \quad (2)$$

where ρ_0 represents the grain/domain boundary effect, $\rho_2 T^2$ is due to the electron–electron scattering and $\rho_{4.5} T^{4.5}$ is attributed to the electron–magnon scattering process in the ferromagnetic region. The experimental data were fitted to the theoretical models in $\rho - T$ plots (not shown). The quality of fitting between them was accessed by the squared linear correlation coefficient (R^2) and a good match between experimental results and theoretical models was obtained. The fitting parameters for all the samples are given in Table 3. It is observed that ρ_0 is greatest among all parameters. This implies that the residual resistivity due to the grain/domain boundary is primarily responsible for the conduction process in the metallic region. Interestingly, the ρ_0 has experienced a drastic increase compared to ρ_2 and $\rho_{4.5}$ as the NiO content increases in composite samples. This observation confirmed that the segregation of NiO at the grain/domain boundary and required electrons to tunnel through the NiO layer during the conduction process. Besides that, it can be seen

that ρ_0 decreases with the application of the magnetic field. This might be attributed to the increase of domain size under the influence of the magnetic field, thus reducing the value of ρ_0 [5]. The polaron conduction is likely to responsible for the conduction in the semiconducting region ($T > T_{MI}$) [37]. The small polaron hopping (SPH) model arising from the strong-phonon coupling due to the Jahn–Teller distortion is given by [38,39]:

$$\rho(T) = \rho_a T \exp(E_a / K_B T) \quad (3)$$

where ρ_a is the temperature-independent coefficient, K_B is Boltzmann's constant and E_a is the activation energy of the polaron. Figure 5 shows the graph of ln (ρ/T) against $1/T$. The plot followed a linear relation at the high-temperature region and the obtained parameters are summarised in Table 3. The good fit between our data and the SPH model demonstrates that the conduction mechanism for the LCMO:NiO composites in the high-temperature region is mainly contributed by the hopping process of small polaron. As shown by the previous studies, the E_a in SPH is related to the height of the phase boundaries [40,41]. It is interesting to point out that the E_a values calculated for the LCMO:NiO composites in this work do not show a significant change with the increasing NiO content. This is contradicted with the previous works as the magnetic disorder in the secondary phase will dominate the conduction process and leads to a higher resistive phase boundary, so a higher E_a is required for the higher concentration of the secondary phase [17,18]. However, the SPH model still accords well with the conduction mechanism in the high-temperature region. Hence, the scattering mechanism in the metallic region can be sufficiently described by the theoretical models as the resistivity data were well fitted with Equations (2) and (3).

Table 3. Parameters obtained corresponding to the best fit of the experimental data based on Equations (2) and (3) for $(1-x)$ LCMO: x NiO (x = 0.00, 0.05, 0.10, 0.15 and 0.20).

NiO Content, x	H (kOe)	$\rho(T) = \rho_0 + \rho_2 T^2 + \rho_{4.5} T^{4.5}$				$\rho(T) = \rho_a T \exp(E_a/K_B T)$	
		ρ_0 (Ω cm)	ρ_2 (Ω cm K^{-2})	$\rho_{4.5}$ (Ω cm K$^{-4.5}$)	R^2	E_a (meV)	R^2
0.00	0	−0.131	0.0047	-9.81×10^{-10}	0.998	1.589	0.999
	10	−1.373	0.0037	-9.00×10^{-10}	0.998	-	-
0.05	0	50.840	0.0133	-4.20×10^{-8}	0.999	1.552	0.998
	10	37.576	0.0102	-3.01×10^{-8}	0.999	-	-
0.10	0	607.812	0.0534	-2.40×10^{-7}	0.999	1.545	0.998
	10	250.109	0.0845	-3.87×10^{-7}	0.997	-	-
0.15	0	-	-	-	-	1.585	0.999
	10	-	-	-	-	-	-
0.20	0	-	-	-	-	1.540	0.997
	10	-	-	-	-	-	-

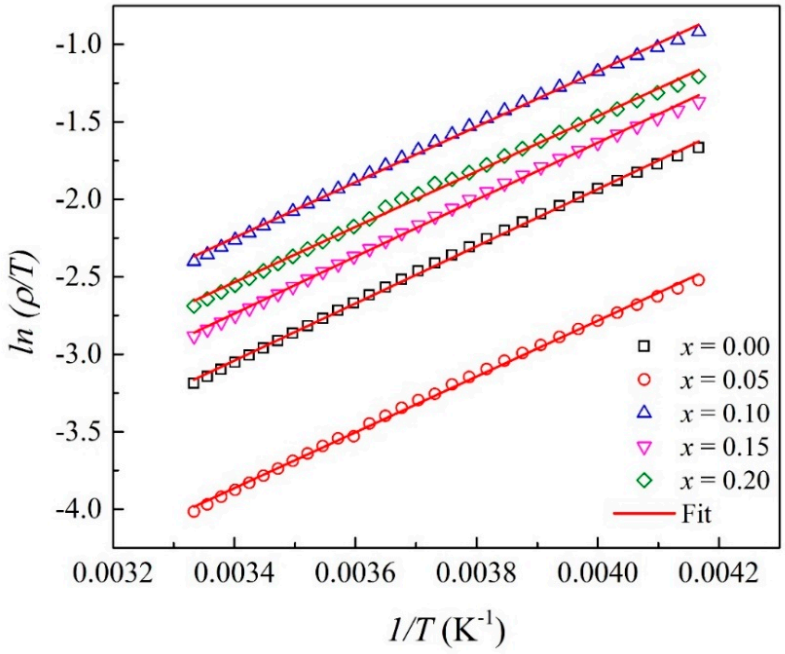

Figure 5. Fitting of resistivity curves of (1−*x*) LCMO: *x* NiO composites by Equation (3).

Figure 6 illustrates the *MR* (%) as a function of external applied magnetic field (0–10 kOe) curves from 80–300 K for (1−*x*) LCMO: *x* NiO, *x* = 0.00, 0.05, 0.10, 0.15 and 0.20. The *MR* (%) is defined by Equation (4):

$$MR\ (\%) = \frac{\rho_H - \rho_O}{\rho_O} \times 100 \quad (4)$$

where ρ_O and ρ_H represent the resistivities without and with an applied magnetic field, respectively. The *MR* (%) curves display two distinct regions as the magnetic field increases. The first region ($H \leq 2$ kOe), better known as LFMR, exhibits a steeper slope in contrast with another part of the curve. The LFMR effect can be attributed to the spin polarised tunnelling across the grain boundaries [11]. The disorder spins in manganite will align when the magnetic field starts to apply, and this causes a drastic drop in resistivity at the low field region due to the electron hopping enhancement. On the other hand, the *MR* (%) increases linearly with the applied magnetic field with a reduced slope in the high field region above 2 kOe. The high field magnetoresistance can be explained by the slow rotation of the grain core and the reduction in the probability of domain-wall scattering with the application of a magnetic field [42,43]. The pure LCMO sample obtained the highest *MR* (%) in this work, which is 29.41% at 80 K (10 kOe). To investigate the variation of magnetic fields on the *MR* (%) of LCMO:NiO composites, plots of *MR* (%) against *T* at 2 kOe and 10 kOe are presented in Figure 7. It is observed that LFMR (2 kOe) is more pronounced at low temperatures by showing a higher value as the temperature decreases. The intrinsic *MR* (%) plot (10 kOe) can be explained by the suppression from spin fluctuations, where the spins are aligned parallel to the magnetic field and exhibit a high *MR* (%) value near the T_{MI} or T_C. As displayed by *MR* (%) curves at 2 kOe, the *MR* (%) of LCMO and its composites increases monotonically with the decrease in temperature and the LFMR was observed. However, the LFMR becomes narrower above 80 K as the NiO content increases and there is no improvement of LFMR contributed by the composites compared with the pure LCMO. In fact, the LFMR originates from the spin polarised tunnelling near the grain boundaries, and grain boundaries can be enhanced through the grain size reduction or the addition of a secondary phase by creating the artificial grain boundaries. The thickness of the grain boundaries created by NiO in this work may exceed the spin memory length and too thick for spin-preserving electron tunnelling [17,44]. As a result, the spin-dependent

tunnelling process is impaired and induces a decrease in LFMR in composite samples. In addition, the thickness of grain boundaries could also be the cause of the fluctuation that happened at *MR* (%) curves at the high-temperature region, as well as the inconsistency of the E_a calculated by SPH fitting in this work compared to previous studies.

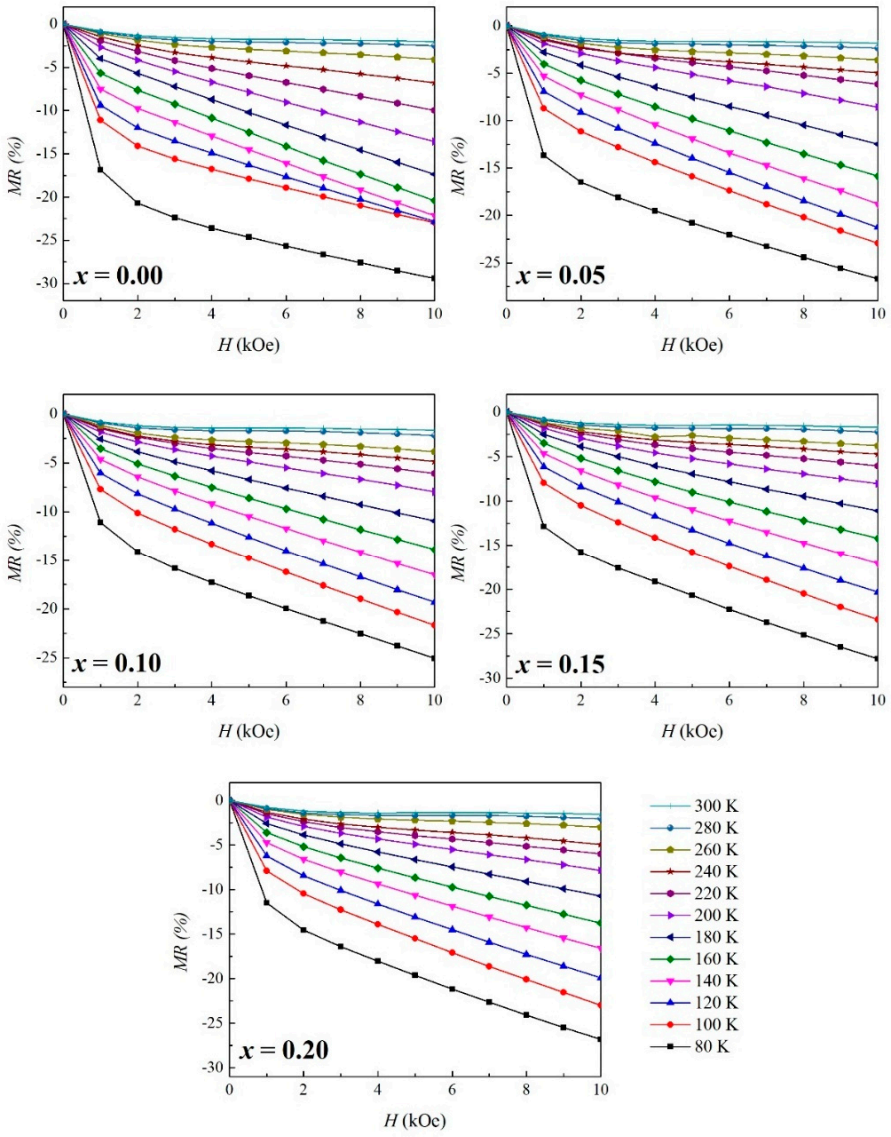

Figure 6. *MR* (%) as a function of external applied magnetic field curves from 80–300 K for (1−*x*) LCMO: *x* NiO, *x* = 0.00, 0.05, 0.10, 0.15 and 0.20.

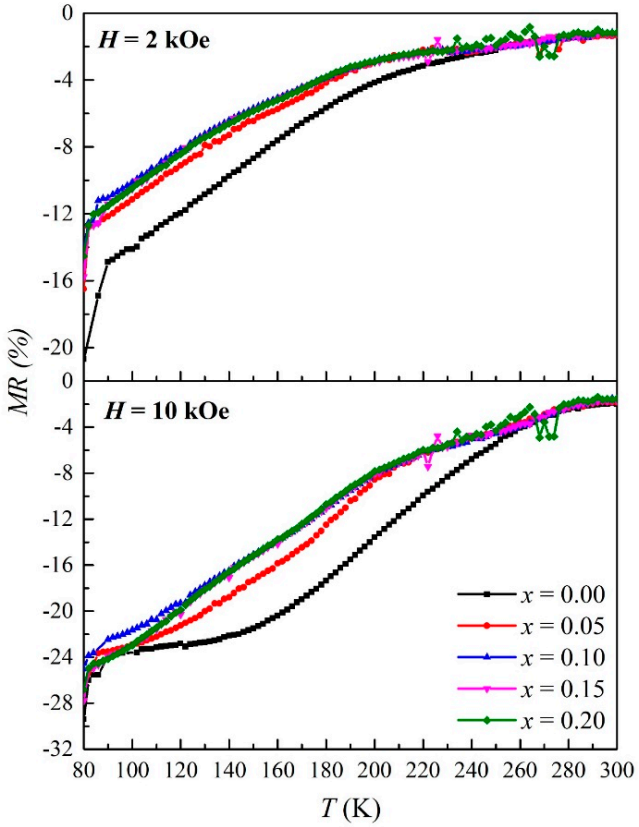

Figure 7. Temperature dependence of *MR* (%) for LCMO:NiO composites at 2 kOe and 10 kOe.

4. Conclusions

The LCMO:NiO composites were successfully synthesised by the sol–gel method. Their structural, microstructural, magnetic, electrical, and magneto-transport properties were systematically studied in this work. The XRD analysis showed that LCMO crystallised into orthorhombic (Pnma) and NiO into cubic (Fm-3m) structures. Both phases coexisted in the composite samples. As NiO content increases, the changes in the lattice constants of composites are insignificant, indicating that NiO was segregated outside the LCMO grains and at the grain boundaries. From microstructural characterisation, the average grain size of composites reduced to ~70 nm with the addition of NiO and confirmed the composite structure of LCMO:NiO. The temperature dependence of AC susceptibility showed double transition for composite samples due to the presence of the antiferromagnetic material (NiO) at the grain boundaries or grain surfaces. The NiO nanoparticle acted as a barrier to charge transport in composites and shifted T_{MI} to lower temperatures. From the theoretical model fitting in the metallic region, the residual resistivity due to the grain/domain boundary is mainly responsible for the conduction process. The LFMR was observed and it is more pronounced at low temperatures. However, there is no improvement of LFMR contributed by the composites compared with the pure LCMO. The concentration of NiO used in this work may create the grain boundary which is larger than the spin memory length and hampered the electron tunnelling process. The findings presented are able to provide some insights into the composite design development especially in the control of secondary phase concentration.

Author Contributions: Conceptualization, L.N.L. and K.P.L.; methodology, L.N.L., S.Y.C. and K.P.L.; validation, L.N.L., S.Y.C., X.T.H., Y.J.W. and A.N.I.; formal analysis, L.N.L., S.Y.C. and K.P.L.; investigation, L.N.L., S.Y.C., X.T.H., Y.J.W. and A.N.I.; resources, K.P.L., M.M.A.K., S.K.C., N.B.I., M.M. (Muralidhar Miryala), M.M. (Masato Murakami) and A.H.S.; writing—original draft preparation, L.N.L.; writing—review and editing, L.N.L. and K.P.L.; visualization, L.N.L. and K.P.L.; supervision, K.P.L., M.M.A.K., S.K.C., N.B.I., M.M. (Muralidhar Miryala), M.M. (Masato Murakami) and A.H.S.;

project administration, K.P.L., M.M.A.K., S.K.C. and A.H.S.; funding acquisition, K.P.L., M.M.A.K., S.K.C., N.B.I. and A.H.S. All authors have read and agreed to the published version of the manuscript.

Funding: This research was fully funded and supported by the Ministry of Higher Education, Malaysia (MOHE), through the Fundamental Research Grant Scheme (FRGS/1/2019/STG07/UPM/02/4) and a Universiti Putra Malaysia (UPM) research grant (GP-IPS/2018/9663900).

Institutional Review Board Statement: Not applicable.

Informed Consent Statement: Not applicable.

Data Availability Statement: The data that support the findings of this study are openly available in Zenodo at http://doi.org/10.5281/zenodo.5089602 (accessed on 10 July 2021).

Acknowledgments: The authors are grateful to the support staff who assisted in the characterisation measurements and for the facilities provided by UPM. L.N. is thankful to the Shibaura Institute of Technology, SIT as the host of aPBL under the Sakura Science Plan and facilitated some of the sample characterisation in this work.

Conflicts of Interest: The authors declare no conflict of interest.

References

1. Mishra, D.; Roul, B.; Singh, S.; Srinivasu, V. Possible observation of Griffith phase over large temperature range in plasma sintered $La_{0.67}Ca_{0.33}MnO_3$. *J. Magn. Magn. Mater.* **2018**, *448*, 287–291. [CrossRef]
2. Panchal, G.; Choudhary, R.J.; Phase, D.M. Magnetic properties of $La_{0.7}Sr_{0.3}MnO_3$ film on ferroelectric $BaTiO_3$ substrate. *J. Magn. Magn. Mater.* **2018**, *448*, 262–265. [CrossRef]
3. Gong, J.; Zheng, D.; Li, D.; Jin, C.; Bai, H. Lattice distortion modified anisotropic magnetoresistance in epitaxial $La_{0.67}Sr_{0.33}MnO_3$ thin films. *J. Alloy. Compd.* **2018**, *735*, 1152–1157. [CrossRef]
4. Xia, W.; Pei, Z.; Leng, K.; Zhu, X. Research progress in rare earth-doped perovskite manganite oxide nanostructures. *Nanoscale Res. Lett.* **2020**, *15*, 1–55. [CrossRef] [PubMed]
5. Ng, S.; Lim, K.; Halim, S.; Jumiah, H. Grain size effect on the electrical and magneto-transport properties of nanosized $Pr_{0.67}Sr_{0.33}MnO_3$. *Results Phys.* **2018**, *9*, 1192–1200. [CrossRef]
6. Zener, C. Interaction between the d-shells in the transition metals. II. Ferromagnetic compounds of manganese with perovskite structure. *Phys. Rev.* **1951**, *82*, 403. [CrossRef]
7. Tang, T.; Tien, C.; Hou, B. Low-field magnetoresistance of Ag-substituted perovskite-type manganites. *Phys. B Condens. Matter* **2008**, *403*, 2111–2115. [CrossRef]
8. Nagaev, E.L. Colossal-magnetoresistance materials: Manganites and conventional ferromagnetic semiconductors. *Phys. Rep.* **2001**, *346*, 387–531. [CrossRef]
9. Sadhu, A.; Bhattacharyya, S. Enhanced low-field magnetoresistance in $La_{0.71}Sr_{0.29}MnO_3$ nanoparticles synthesized by the nonaqueous sol–gel route. *Chem. Mater.* **2014**, *26*, 1702–1710. [CrossRef]
10. Phong, P.T.; Khiem, N.V.; Dai, N.V.; Manh, D.H.; Hong, L.V.; Phuc, N.X. Influence of Al_2O_3 on low-field spin-polarized tunneling magnetoresistance of $(1-x)\ La_{0.7}Ca_{0.3}MnO_3$+x Al_2O_3 composites. *Mater. Lett.* **2009**, *63*, 353–356. [CrossRef]
11. Hwang, H.; Cheong, S.; Ong, N.; Batlogg, a.B. Spin-polarized intergrain tunneling in $La_{2/3}Sr_{1/3}MnO_3$. *Phys. Rev. Lett.* **1996**, *77*, 2041. [CrossRef]
12. Eshraghi, M.; Salamati, H.; Kameli, P. The effect of NiO doping on the structure, magnetic and magnetotransport properties of $La_{0.8}Sr_{0.2}MnO_3$ composite. *J. Alloy. Compd.* **2007**, *437*, 22–26. [CrossRef]
13. Zi, Z.; Fu, Y.; Liu, Q.; Dai, J.; Sun, Y. Enhanced low-field magnetoresistance in LSMO/SFO composite system. *J. Magn. Magn. Mater.* **2012**, *324*, 1117–1121. [CrossRef]
14. Li, J.; Chen, Q.; Yang, S.a.; Yan, K.; Zhang, H.; Liu, X. Electrical transport properties and enhanced broad-temperature-range low field magnetoresistance in LCMO ceramics by Sm_2O_3 adding. *J. Alloy. Compd.* **2019**, *790*, 240–247. [CrossRef]
15. Dar, M.A.; Malla, M.; Solanki, J.; Varshney, D. Enhanced low field magnetoresistance in $La_{0.7}Ca_{0.2}Sr_{0.1}MnO_3$-MgO composites. In *Proceedings of the AIP Conference Proceedings*; American Institute of Physics: College Park, MA, USA, 2017; p. 140013.
16. Thanh, T.D.; Phong, P.T.; Dai, N.V.; Manh, D.H.; Khiem, N.V.; Hong, L.V.; Phuc, N.X. Magneto-transport and magnetic properties of $(1–x)La_{0.7}Ca_{0.3}MnO_3$+$xAl_2O_3$ composites. *J. Magn. Magn. Mater.* **2011**, *323*, 179–184. [CrossRef]
17. Wang, C.B.; Liu, H.X.; Wu, L.; Shen, Q.; Zhang, L.M. Enhanced low-field magnetoresistance in LSMO/AZO composites prepared by plasma activated sintering. *Ceram. Int.* **2018**, *44*, 18048–18053. [CrossRef]
18. Navin, K.; Kurchania, R. Structural, magnetic and transport properties of the $La_{0.7}Sr_{0.3}MnO_3$-ZnO nanocomposites. *J. Magn. Magn. Mater.* **2018**, *448*, 228–235. [CrossRef]
19. Gaur, A.; Varma, G.D. Magnetoresistance behaviour of $La_{0.7}Sr_{0.3}MnO_3$/NiO composites. *Solid State Commun.* **2006**, *139*, 310–314. [CrossRef]

20. Lim, K.P.; Shaari, A.H.; Chen, S.K.; Hassan, J.; Ng, S.W.; Wan Jusoh, W.N.W.; Fadin, N. Electrical Transport Properties and Magnetoresistance of $Pr_{0.67}Sr_{0.33}MnO_3$-NiO Composites. In *Proceedings of the Solid State Phenomena*; Trans Tech Publications Ltd.: Bäch SZ, Switzerland, 2017; pp. 292–296.
21. Ning, X.; Wang, Z.; Zhang, Z. Controllable self-assembled microstructures of $La_{0.7}Ca_{0.3}MnO_3$: NiO nanocomposite thin films and their tunable functional properties. *Adv. Mater. Interfaces* **2015**, *2*, 1500302. [CrossRef]
22. Lau, L.N.; Lim, K.P.; Ngai, L.M.; Ishak, A.N.; Kechik, M.M.A.; Chen, S.K.; Ibrahim, N.B.; Shaari, A.H. Influence of Al_2O_3 on the low-field magnetoresistance of sol–gel grown $La_{0.67}Ca_{0.33}MnO_3$: Al_2O_3 nanocomposites. *Appl. Phys. A* **2020**, *126*, 1–7. [CrossRef]
23. Amri, N.; Nasri, M.; Triki, M.; Dhahri, E. Synthesis and characterization of $(1-x)(La_{0.6}Ca_{0.4}MnO_3)/x$ (Sb_2O_3) ceramic composites. *Phase Transit.* **2019**, *92*, 52–64. [CrossRef]
24. Lim, K.P.; Ng, S.W.; Lau, L.N.; Kechik, M.M.A.; Chen, S.K.; Halim, S.A. Unusual electrical behaviour in sol–gel-synthesised PKMO nano-sized manganite. *Appl. Phys. A* **2019**, *125*, 745. [CrossRef]
25. Xia, W.; Li, L.; Wu, H.; Xue, P.; Zhu, X. Structural, morphological, and magnetic properties of sol-gel derived $La_{0.7}Ca_{0.3}MnO_3$ manganite nanoparticles. *Ceram. Int.* **2017**, *43*, 3274–3283. [CrossRef]
26. Arun, B.; Akshay, V.R.; Chandrasekhar, K.D.; Mutta, G.R.; Vasundhara, M. Comparison of structural, magnetic and electrical transport behavior in bulk and nanocrystalline Nd-lacunar $Nd_{0.67}Sr_{0.33}MnO_3$ manganites. *J. Magn. Magn. Mater.* **2019**, *472*, 74–85. [CrossRef]
27. Navin, K.; Kurchania, R. The effect of particle size on structural, magnetic and transport properties of $La_{0.7}Sr_{0.3}MnO_3$ nanoparticles. *Ceram. Int.* **2018**, *44*, 4973–4980. [CrossRef]
28. Chand, U.; Yadav, K.; Gaur, A.; Varma, G. Magnetic and Magnetotransport Properties of $(Pr_{0.7}Sr_{0.3}MnO_3)1-x/NiOx$ Composites. In Proceedings of the AIP Conference Proceedings; American Institute of Physics: College Park, MA, USA, 2011; pp. 1263–1264.
29. Venkataiah, G.; Venugopal Reddy, P. Electrical behavior of sol–gel prepared $Nd_{0.67}Sr_{0.33}MnO_3$ manganite system. *J. Magn. Magn. Mater.* **2005**, *285*, 343–352. [CrossRef]
30. Staruch, M.; Gao, H.; Gao, P.-X.; Jain, M. Low-field magnetoresistance in $La_{0.67}Sr_{0.33}MnO_3$:ZnO composite film. *Adv. Funct. Mater.* **2012**, *22*, 3591–3595. [CrossRef]
31. Wang, T.; Chen, X.; Wang, F.; Shi, W. Low-field magnetoresistance in $La_{0.7}Sr_{0.3}MnO_3/CuCrO_2$ composites. *Phys. B Condens. Matter* **2010**, *405*, 3088–3091. [CrossRef]
32. De Andres, A.; Garcia-Hernandez, M.; Martinez, J. Conduction channels and magnetoresistance in polycrystalline manganites. *Phys. Rev. B* **1999**, *60*, 7328. [CrossRef]
33. Lau, L.N.; Lim, K.P.; Ishak, A.N.; Awang Kechik, M.M.; Chen, S.K.; Ibrahim, N.B.y.; Miryala, M.; Murakami, M.; Shaari, A.H. The physical properties of submicron and nano-grained $La_{0.7}Sr_{0.3}MnO_3$ and $Nd_{0.7}Sr_{0.3}MnO_3$ synthesised by sol–gel and solid-state reaction methods. *Coatings* **2021**, *11*, 361. [CrossRef]
34. Thombare, B.; Dusane, P.; Kekade, S.; Salunkhe, A.; Choudhary, R.J.; Phase, D.M.; Devan, R.S.; Patil, S.I. Influence of nano-dimensionality on magnetotransport, magnetic and electrical properties of $Nd_{1-x}Sr_xMnO_{3-\delta}$ $(0.3 \leq x \leq 0.7)$. *J. Alloy. Compd.* **2019**, *770*, 257–266. [CrossRef]
35. Li, Y.; Zhang, H.; Chen, Q.; Li, D.; Li, Z.; Zhang, Y. Effects of A-site cationic radius and cationic disorder on the electromagnetic properties of $La_{0.7}Ca_{0.3}MnO_3$ ceramic with added Sr, Pb, and Ba. *Ceram. Int.* **2018**, *44*, 5378–5384. [CrossRef]
36. Mohamed, H. Influence of sodium doping on the electrical and magnetic properties of $La_{0.90}Li_{0.10}MnO_3$ manganites. *J. Magn. Magn. Mater.* **2017**, *424*, 44–52. [CrossRef]
37. Wang, C.B.; Shen, Y.J.; Zhu, Y.X.; Zhang, L.M. Transport properties of $La_{1-x}Sr_xMnO_3$ ceramics above metal–insulator transition temperature. *Phys. B Condens. Matter* **2015**, *461*, 57–60. [CrossRef]
38. Varshney, D.; Dodiya, N. Electrical resistivity of alkali metal doped manganites $La_xA_yMn_wO_3$ (A = Na, K, Rb): Role of electron–phonon, electron–electron and electron–magnon interactions. *Curr. Appl. Phys.* **2013**, *13*, 1188–1198. [CrossRef]
39. Ehsani, M.H.; Kameli, P.; Ghazi, M.E. Influence of grain size on the electrical properties of the double-layered $LaSr_2Mn_2O_7$ manganite. *J. Phys. Chem. Solids* **2012**, *73*, 744–750. [CrossRef]
40. De Teresa, J.; Ibarra, M.; Blasco, J.; Garcia, J.; Marquina, C.; Algarabel, P.; Arnold, Z.; Kamenev, K.; Ritter, C.; Von Helmolt, R. Spontaneous behavior and magnetic field and pressure effects on $La_{2/3}Ca_{1/3}MnO_3$ perovskite. *Phys. Rev. B* **1996**, *54*, 1187. [CrossRef]
41. Ning, X.; Wang, Z.; Zhang, Z. Large, Temperature-tunable low-field magnetoresistance in $La_{0.7}Sr_{0.3}MnO_3$: NiO nanocomposite films modulated by microstructures. *Adv. Funct. Mater.* **2014**, *24*, 5393–5401. [CrossRef]
42. Zhou, Y.; Zhu, X.; Li, S. Structure, magnetic, electrical transport and magnetoresistance properties of $La_{0.67}Sr_{0.33}Mn_{1-x}Fe_xO_3$ (x = 0–0.15) doped manganite coatings. *Ceram. Int.* **2017**, *43*, 3679–3687. [CrossRef]
43. Modi, A.; Bhat, M.A.; Pandey, D.K.; Tarachand; Bhattacharya, S.; Gaur, N.K.; Okram, G.S. Structural, magnetotransport and thermal properties of Sm substituted $La_{0.7-x}Sm_xBa_{0.3}MnO_3$ $(0 \leq x \leq 0.2)$ manganites. *J. Magn. Magn. Mater.* **2017**, *424*, 459–466. [CrossRef]
44. Xiong, C.; Huang, Q.; Xiong, Y.; Ren, Z.; Wei, L.; Zhu, Y.; Li, X.; Sun, C. Electro-magnetic transport behavior of $La_{0.7}Ca_{0.3}MnO_3/SnO_2$ composites. *Mater. Res. Bull.* **2008**, *43*, 2048–2054. [CrossRef]